A Hybrid Ray and Graph Model for Simulating Vehicle-to-Vehicle Channels in Tunnels

Gan, Mingming; Steinböck, Gerhard; Xu, Zhinan; Pedersen, Troels; Zemen, Thomas

Published in:
I E E E Transactions on Vehicular Technology

DOI (link to publication from Publisher):
10.1109/TVT.2018.2839980

Publication date:
2018

Document Version
Accepted author manuscript, peer reviewed version

This article has been accepted for publication in a future issue of this journal, but has not been fully edited. Content may change prior to final publication. Citation information: DOI 10.1109/TVT.2018.2839980, IEEE Transactions on Vehicular Technology

A Hybrid Ray and Graph Model for Simulating Vehicle-to-Vehicle Channels in Tunnels

Mingming Gan, Gerhard Steinböck, Zhinan Xu, Troels Pedersen, Thomas Zemen

***Abstract*—Wave propagation in tunnels for vehicle-to-vehicle (V2V) communications scenarios is characterized by multiple diffuse reflections on tunnel surfaces as well as specular reflections on other objects inside the tunnel, leading to a non-stationary fading process. Such a fading process is difficult to model by ray tracing (RT), requiring a prohibitively high computational complexity due to the large number of diffuse reflections. In this work we propose two new ideas for modeling diffuse reflections in a non-stationary scenarios: (i) We partition the non-stationary fading process into multiple stationarity regions with a given extent in time and frequency for which approximate wide-sense stationarity can be assumed; (ii) we propose a hybrid model, tightly interlinking RT with a propagation graph, such that vertices for the propagation graph are obtained from interaction points calculated by RT for each stationarity region. We compare our hybrid model with measurement data in terms of the time-variant power-delay and the Doppler-power spectral-density as well as the root-mean square delay- and Doppler-spread. This analysis shows, that our hybrid model is the first numerical simulation model that is able to model diffuse reflections inside a tunnel with correct non-stationary (i.e. time-variant) temporal correlation for a non-stationary V2V communication link.**

***Index Terms*—ray tracing, non-stationary fading process, propagation graph, vehicle-to-vehicle, computational complexity.**

I. Introduction

Intelligent transportation systems strongly depend on wireless communication systems for establishing a digital transport infrastructure. Specifically, reliable wireless vehicle-to-vehicle (V2V) communications is important for safety applications including lane change assistance, cooperative forward collision warning, slow vehicle warning, connected autonomous vehicles and more [1]. Therefore, accurate channel models are required for the development, testing and validation of wireless communication systems and standards.

Modeling V2V channels is challenging due to fast-changing propagation conditions, including geometries, variable vehicle speeds and a relatively low height of transmitter (TX) and receiver (RX) antennas. As a consequence the V2V propagation channel differs significantly from typical channels encountered in cellular networks [2], [3]. This is particularly true for the in-tunnel V2V scenario where the semi-enclosed environment gives rise to a large number of diffuse reflections on the tunnel surfaces.

The propagation of VHF and UHF radio signals in tunnels has been addressed in several theoretical and experimental studies as summarized in [4], [5]. Moreover, an excess propagation loss modeling of semi-closed obstacles for intelligent transportation systems has been presented in [6]. Similar to channel models for communication systems in high-speed trains [7], [8], mainly two methodologies have been considered for the V2V scenario:

1) empirical models for summary statistics of the channel, in which typical representatives are the two-slope pathloss channel model [9], [10], and the non-stationary geometry-based stochastic models (GSCMs) [11], [12],
2) deterministic channel models that include ray-based approaches [13]–[17], waveguide models [9], [18], [19] and numerical methods for solving Maxwell's equations [20], [21].

The aims of the two approaches differ significantly: The empirical models for the summary statistics are well suited for overall system design and simplistic simulations, while the deterministic models, which we focus on in this paper, are used to obtain individual channel impulse responses (CIRs) for use in evaluation of system performance.

It is well known that ray tracing (RT) based on the geometrical theory of wave propagation can be applied to model radio wave propagation between a TX and RX [22]. In principle, given a detailed environment description, an accurate prediction can be obtained at the cost of high computational complexity. To reduce the computational complexity of RT it is common to limit the maximum interaction order (i.e. ignoring rays with higher-order interactions) and to consider a simplified environment (e.g. by considering the tunnel to be empty). Both of these approaches are obviously questionable in the V2V tunnel scenario with moving vehicles and static objects such as ventilation systems, doors etc. Hence, to describe V2V propagation channels that account for the complexity of the environment and for rapidly changing propagation conditions a more efficient channel model is required.

A. Literature Review:

In the V2V tunnel scenario, higher order interactions, and in particular higher order reflections, give rise to a 'dense

T. Zemen is with AIT, Austrian Institute of Technology, Vienna, Austria. M. Gan, and Z. Xu have been with AIT, Austrian Institute of Technology, Vienna, Austria while conducting the work of this paper, M. Gan is now with Huawei Technolgies. G. Steinböck and T. Pedersen are with the Dept. of Electronic Systems, Section WCN at Aalborg University, Denmark. The work by M. Gan, Z. Xu and T. Zemen was partly supported by AIT Austrian Institute of Technology in the lead project 'Security & Communication Technologies', and by FTW Forschungszentrum Telekommunikation Wien GmbH in the strategic project 'Diffuse Channel Modeling'. The work by G. Steinböck and T. Pedersen was supported by the cooperative research project VIRTUOSO, funded by Intel Mobile Communications, Telenor, Anite, Aalborg University, and Innovations Fonden Denmark. This work was carried out in the framework of COST Action CA15104 IRACON.

This article has been accepted for publication in a future issue of this journal, but has not been fully edited. Content may change prior to final publication. Citation information: DOI 10.1109/TVT.2018.2839980, IEEE Transactions on Vehicular Technology

multipath component' in the CIR [13]. In this paper we refer to such a dense multipath component as the 'reflection tail'. A similar reflection tail plays an important role in urban crossroads scenarios [2]. The reflection tail of V2V tunnel scenarios was studied in [23], where we proposed a low-complexity RT algorithm for tunnel scenarios by combining RT with an approximate higher-order reflection algorithm. It can be seen that the power of the dense multipath component drops off exponentially with the delay in the early part of the CIR. Unfortunately, this higher-order reflection algorithm is not suitable for modeling the temporal correlation of this 'reflection tail'. Moreover, the tiling algorithm for diffuse walls is not applicable for time-variant scenarios with correlated fading [24].

Recently, a model based on propagation graphs has been proposed to account for the reflection tail in a computationally efficient manner [25], [26]. In fact, closed form expressions are available for reflections of arbitrary order (up to infinity) enabling simulations without the need for limiting the number of interactions. Originally, the propagation graph was considered for indoor propagation, but has since been applied to other scenarios, including high speed railway channels [27] and outdoor-to-indoor scenarios [28]. In [29] the validity of the propagation graph framework has been studied to time-varying channels. This work showed that for velocities encountered in terrestrial settings (including the V2V scenario), the closed form expression for the transfer function a propagation graph can be applied with good approximation. Moreover, for static indoor environments, we recently proposed a hybrid model in [30] which combines deterministic components obtained by RT with a reflection tail modeled by a propagation graph.

Furthermore, a semi-deterministic graph-theory model based on the proven "effective roughness" diffuse scattering theory is proposed in [31]. The main difference between [30] and [31] is the way of generating propagation gain coefficients for dense multipath propagation. The former uses the decay rate, which is predicted with room electromagnetics [32], to set the propagation gain coefficients in the propagation graph, while the latter uses the Lambertian scattering pattern to derive the propagation gain coefficients for double-bounce diffuse scattering situations.

Contributions of the Paper:

We propose a simulation model of the time-varying channel transfer function (CTF) for the V2V tunnel scenario. The model we propose is a hybrid, i.e. a combination of RT and a propagation graph. The purpose of the model is to simulate the time-varying CTF of the V2V channel directly. From this entity other summary statistics such as such as path loss, the distribution of delay spread, or the distribution of the angular spread, can be obtained in a consistent manner.

- We account for the reflection tail by a time-dependent hybrid graph model that is able to model the non-stationary fading processes by using the ray tracing interaction points as vertices of the propagation graph. The PDP decay of the propagation graph is parameterized using the higher-order reflection algorithm [13].
- In [33], it has shown that traffic signs frequently appear along roads and can affect the propagation channel appreciably. However, small or irregularly shaped objects, whose sizes and positions are often not exactly known, are difficult to model by RT. We account for these in the propagation graph in the same manner as done in GSCMs for the mobile radio channel [34], we also include geometry-based discrete scatterers (or point scatterers) for the non-stationary time-variant V2V in-tunnel scenario.
- Our proposed model is the first numerical simulation model that is able to model diffuse reflections inside a tunnel with correct time-variant temporal correlation for a non-stationary V2V communication link.

Organization of the Paper:

The remainder of this contribution is organized as follows. In Section II we describe the hybrid channel model combining RT with a propagation graph. We present RT and propagation graph in Section III and Section IV, respectively. The available measurement data of the tunnel scenario and its time-varying PDP and DSD analysis is introduced in Section V. Simulation results, a comparison to measurements and a discussion of the proposed hybrid algorithm are presented in Section VI. We draw conclusions in Section VII.

II. Hybrid Channel Model

We model the CTF $H(t, f)$ using its sampled representation

$$H[m, q] \triangleq H(mt_\mathrm{s}, f_\mathrm{c} + qf_\mathrm{s}), \tag{1}$$

where m denotes discrete time, q discrete frequency, t_s sampling time, and f_c carrier frequency. The sample spacing in frequency is denoted by $f_\mathrm{s} = B/(Q-1)$, where B denotes the system bandwidth and Q the number of samples in the frequency domain.

We propose a hybrid model for $H[m, q]$ composed of two parts. The first part is RT which computes propagation paths up to a given and limited number of bounces denoted by n_RT. The second part is a propagation graph that accounts for contributions from irregular objects (discrete scatterers) and higher-order reflections. Correspondingly, the CTF of the hybrid model is of the form

$$H[m, q] = H_{\mathrm{RT},0:\mathrm{n_{RT}}}[m, q] + H_{\mathrm{PG},\mathrm{n_{PG}}:\infty}[m, q]. \tag{2}$$

The first part $H_{\mathrm{RT},0:\mathrm{n_{RT}}}[m, q]$, computed by RT, contains LOS, specular reflections up to order $\mathrm{n_{RT}}$, penetration, diffraction, and diffuse scattering. The second part $H_{\mathrm{PG},\mathrm{n_{PG}}:\infty}[m, q]$, computed by the propagation graph, considers the partial response from order $\mathrm{n_{PG}}$ to infinity for calculating the reflection tail and the response related to the contribution from discrete scatterers, which are randomly located on objects with small sizes or irregular shapes. We set $\mathrm{n_{RT}}$ and $\mathrm{n_{PG}}$ according to the rule that the propagation paths obtained from RT and the propagation graph shall not overlap in the delay domain. More details are discussed in Section IV.

This article has been accepted for publication in a future issue of this journal, but has not been fully edited. Content may change prior to final publication. Citation information: DOI 10.1109/TVT.2018.2839980, IEEE Transactions on Vehicular Technology

A. Non-Stationary Fading Process

Vehicular communication channels exhibit a non-stationary fading process due to the mobility of TX, RX and objects in the environment. This non-stationarity was demonstrated by measurements [3], [35] and analyzed using the local scattering function [36]. These investigations show that a general non-stationary fading process in vehicular communication channels can be partitioned into a sequence of local-stationarity regions for which wide-sense-stationarity can be assumed with good accuracy.

The length of a stationarity region influences the computational complexity and the accuracy of both RT and the propagation graph. A shorter stationarity region leads to higher computational complexity and more accurate simulation results. The method presented in [37] can be used to define a stationarity time Mt_s that is matched to different propagation scenario. We relate the global time index m to the stationarity region index $k_\mathrm{t} \in \{1, \ldots, K_\mathrm{t}\}$ according to

$$m = (k_\mathrm{t} - 1)M + m', \tag{3}$$

where $m' \in \{0, \ldots, M-1\}$ expresses the local time index for each stationarity region k_t.

Here we use a stationarity region oriented calculation of the channel model, hence we rewrite (2) as

$$H[m', q, k_\mathrm{t}] = H_{\mathrm{RT},0:\mathrm{n_{RT}}}[m', q, k_\mathrm{t}] + H_{\mathrm{PG},\mathrm{n_{PG}}:\infty}[m', q, k_\mathrm{t}]\,, \tag{4}$$

partitioning the fading process into consecutive stationarity regions indexed by k_t.

The hybrid modeling procedure for obtaining a CTF for one stationary region is illustrated in the block diagram in Fig. 1 and detailed in the following sections.

III. Ray Tracing (RT)

Our RT tool is three-dimensional (3D), where the geometry is described in a cartesian coordinate system and the simulation environment is generated using perpendicular parallelepiped elements. The input of RT includes the geometric scenario, network layout and antenna parameters. RT calculates a set of propagation paths connecting the TX and the RX based on geometric and electromagnetic computations. The geometric computations determine the propagation paths interacting with the environment, while the electromagnetic computations provide the electric field of all propagation paths in amplitude, phase and polarization.

RT considers three major wave propagation mechanisms: (i) line of sight (LOS), (ii) specular contributions and (iii) diffuse scattering. The specular contributions include reflection, penetration and diffraction components. For paths based on the LOS and specular contributions, we use the term deterministic paths. The geometrical relationship of a deterministic path is based on optical principles [38]. Complex dyadic coefficients for reflection and penetration are obtained using Fresnel formulas, while the diffraction coefficient is calculated by the uniform theory of diffraction (UTD) [39]. A directive pattern model, assuming that the scattering lobe is steered toward the direction of the specular reflection, is used to model the contribution of the diffuse part of the channel impulse response [40].

In order to save simulation time needed for the computation of diffuse scattering paths, a subdivision algorithm based on concentric circles is applied, which significantly reduces the computational complexity of RT with no loss in accuracy [41]. This algorithm assumes that diffuse scattering tiles are equally sized circular segments within the same radius Δd on a certain surface and the relevant path originates from the center of each tile. We set the tile size to

$$dS = \pi \cdot \Delta d^2 = \pi \cdot \left(\frac{c}{2 \cdot B}\right)^2, \tag{5}$$

where B is the system bandwidth. It is known that the delay resolution $\Delta\tau = 1/B$. Therefore, this calculation means that the distance between any two circular tile centers on one surface is not shorter than the distance between two diffuse scattering paths which are located in two adjacent delay bins. The diffuse scattering tiles are kept constant for each stationarity region k_t. The weighting coefficient

$$\eta_\ell[0, k_\mathrm{t}] = \sqrt{|\eta_{\ell_\mathrm{max}}[0, k_\mathrm{t}]|^2 \cdot \left(\frac{1 + \cos(\varphi_\ell[0, k_\mathrm{t}])}{2}\right)^\alpha}\, e^{-\mathrm{i}\theta_\ell[k_\mathrm{t}]}, \tag{6}$$

where ℓ is the diffuse scattering tile index, $\eta_{\ell_\mathrm{max}}[m', k_\mathrm{t}]$ is the maximum amplitude [40] related to the $\ell-$th scattering lobe, $\varphi_\ell[m', k_\mathrm{t}]$ is the angle between the $\ell-$th scattering wave and the $\ell-$th reflection wave directions, α is an integer defining the width of the scattering lobe and $\theta_\ell[k_\mathrm{t}]$ is the random phase associated with the $\ell-$th path with a uniform distribution within $[0, 2\pi]$. We randomly draw θ_ℓ once for each stationarity region.

A. Reflection Tail

In [23], we show that the 'reflection tail', modeled as the combined power of higher-order reflection paths, drops off exponentially with delay. This exponential decay can be simulated with a large number of higher-order reflection paths. However, the computational complexity of RT, i.e. its runtime on a given hardware, increases exponentially with the reflection order.

RT performs two main steps to calculate the reflection paths: i) the visibility procedure and ii) the back track procedure. The visibility procedure builds up the image tree and the back track procedure helps to determine the existing reflection paths. Our RT tool saves only the information related to the existing reflection paths in the image tree, but the computational complexity involved in the back track procedure still increases exponentially with the reflection order. In [23], we considered to model the reflection tail for complexity reasons with the approximate higher order reflection algorithm. However, this algorithm does not capture the Doppler behavior appropriately. Therefore, we introduce the propagation graph to model the reflection tail, see (2).

For the RT part $H_{\mathrm{RT},0:\mathrm{n_{RT}}}[m, q, k_\mathrm{t}]$ we limit the maximum reflection order of a reflected path with $\mathrm{n_{RT}}$ and we consider single order diffraction and single order diffuse scattering contributions. Higher order reflections will be modeled using the propagation graph $H_{\mathrm{PG},\mathrm{n_{PG}}:\infty}[m, q, k_\mathrm{t}]$, see Section IV.

This article has been accepted for publication in a future issue of this journal, but has not been fully edited. Content may change prior to final publication. Citation information: DOI 10.1109/TVT.2018.2839980, IEEE Transactions on Vehicular Technology

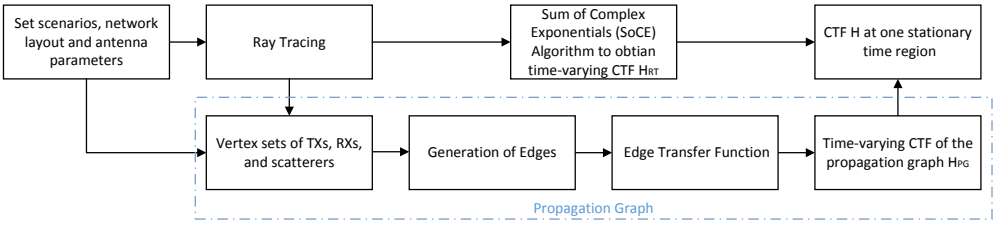

Fig. 1. The procedure of hybrid channel model at one stationary time region.

B. Sum of Complex Exponentials (SoCE) Algorithm

We reduce the complexity of RT by applying the SoCE algorithm [38] for each stationarity region. The SoCE algorithm relies on the assumption that within one stationarity region, the magnitude of each ray remains constant and only the phase changes. Thus, for the time-variant CTF of RT $H_{\mathrm{RT}}[m', q, k_{\mathrm{t}}]$, we first calculate the RT results for the initial time index $m' = 0$. Then we use the SoCE algorithm to calculate the time-varying CTF

$$H_{\mathrm{RT},0:\mathrm{n_{RT}}}[m', q, k_{\mathrm{t}}] = \sum_{l=1}^{L_{\mathrm{RT}}[k_{\mathrm{t}}]} \eta_l[0, k_t] e^{-\mathrm{i}2\pi q f_{\mathrm{s}} \tau_l[0,k_{\mathrm{t}}]} \cdot e^{\mathrm{i}2\pi m' t_{\mathrm{s}} \nu_l[0,k_{\mathrm{t}}]}, \quad (7)$$

for $m' \in \{0, \ldots, M-1\}$, where l is the propagation path index, $L_{\mathrm{RT}}[k_{\mathrm{t}}]$ is the total number of propagation paths for stationarity region k_{t}, $\eta_l[m', k_{\mathrm{t}}]$, $\tau_l[m', k_{\mathrm{t}}]$ and $\nu_l[m', k_{\mathrm{t}}]$ denote complex path weight, delay and Doppler shift of the $l-$th path, respectively. The Doppler shift [1] at the center frequency f_{c} is given as [42]

$$\nu_l[0, k_{\mathrm{t}}] = (|v_{\mathrm{RX}}| \cos(\phi_l[0, k_{\mathrm{t}}]) + |v_{\mathrm{TX}}| \cos(\beta_l[0, k_{\mathrm{t}}])) f_{\mathrm{c}}/c, \quad (8)$$

where c is the speed of light, $\phi_l[m', k_{\mathrm{t}}]$ is the angle between the direction of movement of the RX and the line connecting the $l-$th interaction point with the RX and $\beta_l[m', k_{\mathrm{t}}]$ is the angle between the direction of movement of the TX and the line connecting the $l-$th interaction point with the TX.

IV. Propagation Graph

To account for the reflection tail, we rely on propagation graph theory [26]. The propagation environment is represented as a directed graph $\mathcal{G} = (\mathcal{V}, \mathcal{E})$ with vertices denoting TXs, RXs or scatterers and edges denoting propagation conditions between vertices. The signals propagate via the edges of the directed graph. Each TX emits a signal via the outgoing edges, while a RX sums up the signals arriving via the ingoing edges. A scatterer sums up the signals on its ingoing edges and re-emits the sum on its outgoing edges.

The structure of a propagation graph is particular. The vertex set is partitioned into sets of TXs, RXs, and scatterers, respectively, as $\mathcal{V} = \mathcal{V}_{\mathrm{TX}} \cup \mathcal{V}_{\mathrm{RX}} \cup \mathcal{V}_{\mathrm{S}}$. Consequently, the edge set $\mathcal{E}$ can be partitioned into four subsets: the TX-RX edge subset $\mathcal{E}_{\mathrm{TR}}$, the TX-scatterer edge subset $\mathcal{E}_{\mathrm{TS}}$, the scatterer-RX edge subset $\mathcal{E}_{\mathrm{SR}}$, and the scatterer-scatterer edge subset $\mathcal{E}_{\mathrm{SS}}$.

[1]The Doppler shift due to moving object is negligible here, because the moving object is considered in the propagation graph.

To each edge $e \in \mathcal{E}$, we associate a transfer function denoted by $A_e[q, k_{\mathrm{t}}]$. These transfer functions are collected in the weighted adjacency matrix $\mathbf{A}[q, k_{\mathrm{t}}]$ which is a complex matrix of dimension $(N_{\mathrm{TX}} + N_{\mathrm{RX}} + N_{\mathrm{S}}) \times (N_{\mathrm{TX}} + N_{\mathrm{RX}} + N_{\mathrm{S}})$, where N_{TX}, N_{RX} and N_{S} are the number of TXs, RXs and scatterers considered in the propagation graph. The propagation graph's structure carries over to its weighted adjacency matrix which takes the form

$$\mathbf{A}[q, k_{\mathrm{t}}] = \begin{bmatrix} \mathbf{0} & \mathbf{0} & \mathbf{0} \\ \mathbf{D}[q, k_{\mathrm{t}}] & \mathbf{0} & \mathbf{R}[q, k_{\mathrm{t}}] \\ \mathbf{T}[q, k_{\mathrm{t}}] & \mathbf{0} & \mathbf{B}[q, k_{\mathrm{t}}] \end{bmatrix}. \quad (9)$$

Here, $\mathbf{0}$ denotes the all-zero matrix of the appropriate dimension and the transfer matrices

$$\begin{array}{lllll} \mathbf{D}[q, k_{\mathrm{t}}] \in \mathbb{C}^{N_{\mathrm{RX}} \times N_{\mathrm{TX}}}: & \text{transmitters} & \rightarrow & \text{receivers}, \\ \mathbf{R}[q, k_{\mathrm{t}}] \in \mathbb{C}^{N_{\mathrm{RX}} \times N_{\mathrm{S}}}: & \text{scatterers} & \rightarrow & \text{receivers}, \\ \mathbf{T}[q, k_{\mathrm{t}}] \in \mathbb{C}^{N_{\mathrm{S}} \times N_{\mathrm{TX}}}: & \text{transmitters} & \rightarrow & \text{scatterers}, \\ \mathbf{B}[q, k_{\mathrm{t}}] \in \mathbb{C}^{N_{\mathrm{S}} \times N_{\mathrm{S}}}: & \text{scatterers} & \rightarrow & \text{scatterers}. \end{array}$$

As shown in [26], the full and partial transfer functions, accounting for propagation paths with an unbounded interaction order, can be expressed in closed form. Appendix A states expressions for the transfer function $\mathbf{H}_{\mathrm{PG}}[q, k_{\mathrm{t}}]$ and the partial transfer functions $\mathbf{H}_{\mathrm{PG},K:\infty}[q, k_{\mathrm{t}}]$ from K to an infinite number of bounces.

A. Propagation Graph for the V2V Tunnel Scenario

The general propagation graph structure, is now specialized for V2V tunnel scenario considered here. The structure of the propagation graph unfolds in the vector signal flow graph depicted in Fig. 2. To each vertex we associate a three-dimensional geometrical position. This enable us to define propagation delays of edges according to the geometric distance between the start and end vertices. We define one propagation graph per stationarity region. To capture the movement of TX and RX along their trajectories at the M sample times within a stationarity region, we consider sets of TXs $\mathcal{V}_{\mathrm{TX}} = \{\mathrm{TX}_0, \ldots, \mathrm{TX}_{M-1}\}$ and the set of RXs $\mathcal{V}_{\mathrm{RX}} = \{\mathrm{RX}_0, \ldots, \mathrm{RX}_{M-1}\}$. The positions of scatterer vertices $\mathcal{V}_{\mathrm{S}}$ in the graph are obtained from the geometric RT results and the geometrical description of the scenario.

The set of scatterers can be partitioned as $\mathcal{V}_{\mathrm{S}} = \mathcal{V}_{\mathrm{IP}} \cup \mathcal{V}_{\mathrm{SD}} \cup \mathcal{V}_{\mathrm{MD}}$, where the 'interaction points (IPs)' $\mathcal{V}_{\mathrm{IP}}$ are directly obtained by the RT reflection points. The 'static discrete (SD) scatterers' $\mathcal{V}_{\mathrm{SD}}$ are located on significant static objects in the tunnel, and 'mobile discrete (MD) scatterers'

This article has been accepted for publication in a future issue of this journal, but has not been fully edited. Content may change prior to final publication. Citation information: DOI 10.1109/TVT.2018.2839980, IEEE Transactions on Vehicular Technology

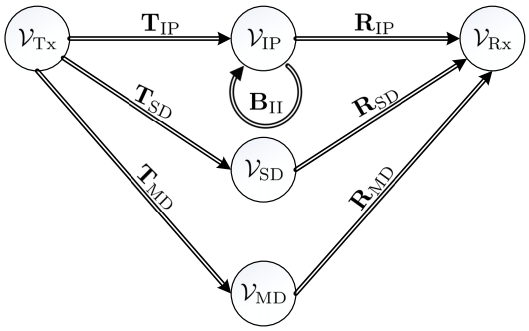

Fig. 2. Vector signal flow graph representation of the proposed propagation graph in tunnel scenarios.

$\mathcal{V}_{\mathrm{MD}}$ are located on moving objects in the tunnel. These static and moving objects, whose sizes, positions and irregular shapes are not exactly known, are made of metal or glass. Hence, these objects are important reflectors or scatterers, but they are hard to describe in RT. Therefore, we consider the contributions from these objects in the propagation graph. We update $\mathcal{V}_{\mathrm{IP}}$ and $\mathcal{V}_{\mathrm{SD}}$ positions once for the beginning of each stationarity region k_{t}. Within one stationarity region k_{t}, we use the fixed $\mathcal{V}_{\mathrm{IP}}$ and $\mathcal{V}_{\mathrm{SD}}$ positions for all time indeces $m' \in \{0, \ldots, M-1\}$, while for the $\mathcal{V}_{\mathrm{MD}}$, we update the MD positions for each time index m' according to their velocity. The time-varying transfer function of the propagation graph[1]

$$H_{\mathrm{PG}}[m', q, k_{\mathrm{t}}] = \mathbf{r}[m', q, k_{\mathrm{t}}]\mathbf{B}^{\mathrm{n_{PG}}-1}[q, k_{\mathrm{t}}] \times [\mathbf{I} - \mathbf{B}[q, k_{\mathrm{t}}]]^{-1}\mathbf{t}[m', q, k_{\mathrm{t}}] \quad (10)$$

accounts for interactions from $\mathrm{n_{PG}}$ to infinity where $\mathbf{r}[m', q, k_{\mathrm{t}}]$ is the $m'-$th row vector of $\mathbf{R}[q]$ and $\mathbf{t}[m', q, k_{\mathrm{t}}]$ is the $m'-$th column vector of $\mathbf{T}[q]$. The reason is that we are not interested in the transfer function between all pairs of M TXs and M RXs. We are only interested in the ones with the same index m' to emulate the movement of the single antenna at the TX and RX.

The edges of the propagation graph are defined by considering the specific geometry of the tunnel scenario. We assume that there is no edges between different scatterer types. The reason is, that we treat the contribution from either a SD or a MD scatterer to be a single interaction path, in the same way as the contributions from single objects in the tunnel which are observed in the measurements shown in Fig. 6(a). This structures the submatrices $\mathbf{T}[q, k_{\mathrm{t}}]$, $\mathbf{R}[q, k_{\mathrm{t}}]$, and $\mathbf{B}[q, k_{\mathrm{t}}]$ according to

$$\mathbf{T}[q, k_{\mathrm{t}}] = \begin{bmatrix} \mathbf{T}_{\mathrm{IP}}[q, k_{\mathrm{t}}] \\ \mathbf{T}_{\mathrm{SD}}[q, k_{\mathrm{t}}] \\ \mathbf{T}_{\mathrm{MD}}[q, k_{\mathrm{t}}] \end{bmatrix}, \quad (11)$$

$$\mathbf{R}[q, k_{\mathrm{t}}] = \begin{bmatrix} \mathbf{R}_{\mathrm{IP}}[q, k_{\mathrm{t}}] & \mathbf{R}_{\mathrm{SD}}[q, k_{\mathrm{t}}] & \mathbf{R}_{\mathrm{MD}}[q, k_{\mathrm{t}}] \end{bmatrix} \quad (12)$$

and

$$\mathbf{B}[q, k_{\mathrm{t}}] = \begin{bmatrix} \mathbf{B}_{\mathrm{II}}[q, k_{\mathrm{t}}] & \mathbf{0} & \mathbf{0} \\ \mathbf{0} & \mathbf{0} & \mathbf{0} \\ \mathbf{0} & \mathbf{0} & \mathbf{0} \end{bmatrix} \quad (13)$$

[1]The LOS contribution is included in RT, so $\mathbf{D} = \mathbf{0}_{M \times M}$

with the definitions

$\mathbf{T}_{\mathrm{IP}}[q, k_{\mathrm{t}}] \in \mathbb{C}^{N_{\mathrm{IP}} \times M}$: transmitters $\rightarrow$ IP scatterers,
$\mathbf{T}_{\mathrm{SD}}[q, k_{\mathrm{t}}] \in \mathbb{C}^{N_{\mathrm{SD}} \times M}$: transmitters $\rightarrow$ SD scatterers,
$\mathbf{T}_{\mathrm{MD}}[q, k_{\mathrm{t}}] \in \mathbb{C}^{N_{\mathrm{MD}} \times M}$: transmitters $\rightarrow$ MD scatterers,
$\mathbf{R}_{\mathrm{IP}}[q, k_{\mathrm{t}}] \in \mathbb{C}^{M \times N_{\mathrm{IP}}}$: IP scatterers $\rightarrow$ receivers,
$\mathbf{R}_{\mathrm{SD}}[q, k_{\mathrm{t}}] \in \mathbb{C}^{M \times N_{\mathrm{SD}}}$: SD scatterers $\rightarrow$ receivers,
$\mathbf{R}_{\mathrm{MD}}[q, k_{\mathrm{t}}] \in \mathbb{C}^{M \times N_{\mathrm{MD}}}$: MD scatterers $\rightarrow$ receivers,
$\mathbf{B}_{\mathrm{II}}[q, k_{\mathrm{t}}] \in \mathbb{C}^{N_{\mathrm{IP}} \times N_{\mathrm{IP}}}$: IP scatterers $\rightarrow$ IP scatterers,

where N_{IP}, N_{SD} and N_{MD} are the number of IPs, SD and MD scatterers considered in the propagation graph, and $N_{\mathrm{S}} = N_{\mathrm{IP}} + N_{\mathrm{SD}} + N_{\mathrm{MD}}$.

We remark that the structure of $\mathbf{B}[q, k_{\mathrm{t}}]$ and the fact that the matrices $\mathbf{B}_{\mathrm{II}}[q, k_{\mathrm{t}}]$ is constant for the duration of a stationarity region k_{t} simplifies the computation in (10).

B. Generation of Edges

The edges of the propagation graph are defined according to their type as listed in Table I and explained below. We follow the principle to permit no edge between scatterers on the same surface. Thus a tunnel wall does not scatter signal back onto itself. Furthermore, we generate edges according to the rules

- We exclude TX-RX edges (the LOS contribution is included in RT).
- Edges of the types SD-SD and MD-MD are excluded since we consider only single interactions from SD and MD scatterers.
- Edges of the types TX-SD, TX-MD, SD-RX, and MD-RX are always included.
- Edges of the types TX-IP and IP-RX are included in the graph with randomly and independent with probability P_{vis}.
- An IP-IP edge (from scatterer i to j at positions $\mathbf{r}_{\mathrm{i}'}$ and $\mathbf{r}_{\mathrm{j}'}$) is included if the following conditions are fulfilled:

$$d_{\mathrm{th,min}} \leq \|\mathbf{r}_{\mathrm{i}'} - \mathbf{r}_{\mathrm{j}'}\| \leq d_{\mathrm{th,max}}, \quad (14)$$

$$\|\mathbf{r}_{\mathrm{TX}} - \mathbf{r}_{\mathrm{i}'}\| + \|\mathbf{r}_{\mathrm{i}'} - \mathbf{r}_{\mathrm{j}'}\| + \|\mathbf{r}_{\mathrm{RX}} - \mathbf{r}_{\mathrm{j}'}\| \geq d_{\mathrm{ref,max}}, \quad (15)$$

where $\|\cdot\|$ is the Euclidean norm, $d_{\mathrm{th,min}}$ and $d_{\mathrm{th,max}}$ are the minimum and maximum distance thresholds, and $d_{\mathrm{ref,max}}$ is the longest reflection path calculated by RT.

The condition (14) ensures that scatterers should not be either too close or too far away from each other. The condition (15) ensures that propagation paths obtained from the RT does not overlap in delay with paths obtained from the propagation graph.

C. Edge Transfer Function

The edge transfer function for a pair of vertices $e = (v, v')$ is defined according to

$$A_e[q, k_{\mathrm{t}}] = \begin{cases} g_e[q, k_{\mathrm{t}}] \exp(-\mathrm{i}2\pi\tau_e f[q]), & e \in \mathcal{E}, \\ 0, & e \notin \mathcal{E}, \end{cases} \quad (16)$$

where $g_e[q]$ denotes the 'edge gain' and $\tau_e = \tau_{(v,v')} = \|\mathbf{r}_v - \mathbf{r}_{v'}\|/c$ is the propagation delay, and the q-th frequency is defined as $f[q] = f_{\mathrm{c}} + q f_{\mathrm{s}}$.

Table I defines the edge gains. The gain of the direct TX-RX edge is defined according to the Friis equation. The gains of the TX-IP, TX-SD, TX-MD, IP-RX, SD-RX and MD-RX

This article has been accepted for publication in a future issue of this journal, but has not been fully edited. Content may change prior to final publication. Citation information: DOI 10.1109/TVT.2018.2839980, IEEE Transactions on Vehicular Technology

TABLE I
EDGE GAINS AND PROBABILITY OF VISIBILITY WITHIN STATIONARITY REGION

Edge type	Edge Precense	Edge gain (g_e)	Submatrix
TX–RX	No	—	($\mathbf{D}=\mathbf{0}$)
TX–IP	Independent w. prob. P_{vis}	$\left(\frac{1}{4\pi f[q]\tau_{(v\times v'\times v'')}}\right)^{\frac{1}{2}}$	$\mathbf{T}_{\text{IP}}$
TX–SD	Yes	$\left(\frac{S_{e,\text{TS}}}{4\pi f[q]\tau_{(v\times v'\times v'')}}\right)^{\frac{1}{2}}$	$\mathbf{T}_{\text{SD}}$
TX–MD	Yes	$\left(\frac{S_{e,\text{TM}}}{4\pi f[q]\tau_{(v\times v'\times v'')}}\right)^{\frac{1}{2}}$	$\mathbf{T}_{\text{MD}}$
IP–IP	According to (14) & (15).	$g_{\text{II}}\sqrt{S_{e,\text{II}}}e^{j\theta_{\text{II}}}$	$\mathbf{B}_{\text{II}}$
IP–RX	Independent w. prob. P_{vis}	$\left(\frac{1}{4\pi f[q]\tau_{(v\times v'\times v'')}}\right)^{\frac{1}{2}}$	$\mathbf{R}_{\text{IP}}$
SD–RX	Yes	$\left(\frac{S_{e,\text{SR}}}{4\pi f[q]\tau_{(v\times v'\times v'')}}\right)^{\frac{1}{2}}$	$\mathbf{R}_{\text{SD}}$
MD–RX	Yes	$\left(\frac{S_{e,\text{MR}}}{4\pi f[q]\tau_{(v\times v'\times v'')}}\right)^{\frac{1}{2}}$	$\mathbf{R}_{\text{MD}}$
Other edge types	No	—	—

Note: $\tau_{(v\times v'\times v'')}$ computed according to (17).

edges, are defined so that the total gain of a TX-scatterer-RX path resembles the Friis equation considering first order interactions. To this end, we denote the propagation delay as

$$\tau_{(v\times v'\times v'')} = \tau_{(v,v')} + \tau_{(v',v'')}, \tag{17}$$

where $v \in \mathcal{V}_{\text{TX}}$, $v' \in \mathcal{V}_{\text{S}}$ and $v'' \in \mathcal{V}_{\text{RX}}$ (see Table I). Moreover, we define the edge weight according to

$$S_{e,\{\cdot\}} = \begin{cases} \frac{1}{\sqrt{\text{odi}_{\{\cdot\}}(e)}}, & \{\cdot\} \in \{\text{TS},\text{TM},\text{II}\}, \\ \frac{1}{\sqrt{\text{idi}_{\{\cdot\}}(e)}}, & \{\cdot\} \in \{\text{SR},\text{MR}\}, \end{cases} \tag{18}$$

where $\text{odi}_{\{\cdot\}}(e)$ is the number of outgoing edges of the vertex and $\text{idi}_{\{\cdot\}}(e)$ is the number of ingoing edges of the vertex[3].

The gain of IP-IP edges, is defined as in [26] and is related to the slope ρ of the power-delay spectrum of the higher-order reflection paths as

$$g_{\text{II}} \approx 10^{\frac{\rho\mu(\mathcal{E}_{\text{II}})}{20}}, \tag{19}$$

where $\mu(\mathcal{E}_{\text{II}}) = \frac{1}{|\mathcal{E}_{\text{II}}|}\sum_{e\in\mathcal{E}_{\text{II}}}\tau(e \in \mathcal{E}_{\text{II}})$ is the average delay among all edges $e \in \mathcal{E}_{\text{II}}$. The phase θ_{II}, shown in Table I, is uniformly distributed over $[0, 2\pi]$ and is set only once for each stationarity region. The slope ρ can be set empirically based on measurement results or predicted with numerous methods. In [30] we considered room electromagnetics. For a tunnel, which is oddly shaped compared to a 'regular' room and has open ends, the standard room electromagnetic formulas are not well suited. Instead we predict the slope ρ with the approximate higher-order reflection algorithm for $m' = 0$. Please see Appendix C for more details. The wave guiding effect, which is an important propagation phenomenon in tunnel scenarios, is accounted for when setting the slope value ρ as follows. After obtaining the CIR based on the approximate higher-order reflection algorithm, a least-squares linear regression line is superimposed on the delay-power spectrum plot to obtain the slope ρ in (19), see Fig. 5.

[3]This definition is based on the assumption that the transmitted power or the received power is distributed into the outgoing or ingoing edges equally, respectively. If more accurate results are required, a modified definition of the edge weight might be needed. However, this is beyond the scope of this paper.

V. IN-TUNNEL MEASUREMENTS AND TIME-VARYING ANALYSIS

A. In-Tunnel Measurements

The measurements used in the present work were collected in the DRIVEWAY'09 measurement campaign [43] in the Øresund tunnel connecting Denmark and Sweden. The measurements started when the TX driving in front of the RX enters the tunnel. The RX enters the tunnel at $t = 2\,\text{s}$. The picture in Fig. 3 is taken from the video of the measurements when both, the TX- and the RX-vehicle, are inside the tunnel. The distance between both vehicles is about $d = 120\,\text{m}$ and their speed is kept approximately constant at $v_{\text{RX}} = v_{\text{TX}} = 105\,\text{km/h}$ for the measurement time interval of $10\,\text{s}$.

Each vehicle is equipped with a four element linear array of circular patch antennas mounted on the roof perpendicular to the driving direction. The antenna array was specifically designed for high-resolution mobile-to-mobile channel measurements [44]. The main lobe of each antenna element is oriented in one of four directions: left, right, back and front, thus the antenna array covers 360° in the azimuthal plane. The antenna gain remains on average within a variation of 10 dB for the whole bandwidth.

The channel transfer function (CTF) $H(t, f)$ is measured over a time interval of $T = 10\,\text{s}$, which contains $S =$

This article has been accepted for publication in a future issue of this journal, but has not been fully edited. Content may change prior to final publication. Citation information: DOI 10.1109/TVT.2018.2839980, IEEE Transactions on Vehicular Technology

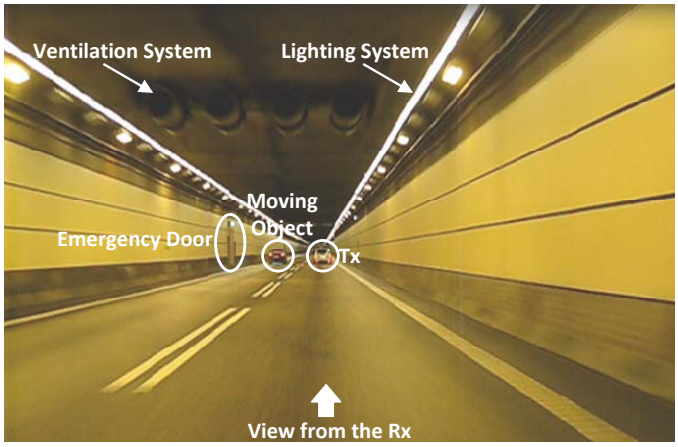

Fig. 3. Video snapshot representing measurement environment.

32000 time snapshots with a snapshot repetition time of $t_\mathrm{s} = 307.2\,\mu\mathrm{s}$. There are $Q = 769$ frequency samples in the measurement bandwidth of $B = 240\,\mathrm{MHz}$, where the carrier frequency $f_\mathrm{c} = 5.6\,\mathrm{GHz}$. These parameters result in a resolution in the frequency domain of $f_\mathrm{s} = B/(Q-1) = 312.5\,\mathrm{kHz}$. This parameterization is used also for the numerical evaluation of the hybrid channel model.

We sample the time-varying CTF according to

$$H_\iota[m,q] \triangleq H_\iota(mt_\mathrm{s}, f_\mathrm{c} + qf_\mathrm{s}), \tag{20}$$

where $\iota \in \{1,\ldots,\mathcal{L}\}$ is the link index with $\mathcal{L} = 16$ for our case, $m \in \{0,\ldots,S-1\}$ is the discrete time (and snapshot) index, $q \in \{-\lfloor \frac{Q}{2} \rfloor, \ldots, \lfloor \frac{Q}{2} \rfloor - 1\}$ is the sampled frequency index and $\lfloor \cdot \rfloor$ indicates the floor function. We sum over all CTFs within one snapshot to approximate an omnidirectional antenna radiation pattern

$$H[m,q] = \frac{1}{\mathcal{L}} \sum_{\iota=1}^{\mathcal{L}} H_\iota[m,q]. \tag{21}$$

B. Local Scattering Function Based Measurements Analysis

The local scattering function (LSF), a short-term representation of the power spectrum of the observed fading process, is a useful tool for characterizing non-stationary time-variant channels [1], [36]. We assume the fading process is locally stationary within a stationarity region with size $M \times N$ samples in time and frequency, respectively. In order to calculate the LSF, we index the stationarity regions in time $k_\mathrm{t} \in \{1,\ldots,\lfloor S/M \rfloor\}$ and frequency $k_\mathrm{f} \in \{1,\ldots,\lfloor Q/N \rfloor\}$ obtaining a total of $\lfloor S/M \rfloor \lfloor Q/N \rfloor$ stationarity regions. The estimate of the discrete LSF is denoted as [45], [37]

$$\hat{\mathcal{C}}[k_\mathrm{t},k_\mathrm{f};n,p] = \frac{1}{IJ} \sum_{w=0}^{IJ-1} \left| \mathcal{H}^{(\mathbf{G}_w)}[k_\mathrm{t},k_\mathrm{f};n,p] \right|^2, \tag{22}$$

where $n \in \{0,\ldots,N-1\}$ denotes the delay index, $p \in \{-M/2,\ldots,M/2-1\}$ the Doppler index, I is the number of orthogonal time-domain tapers, J is the number of orthogonal frequency-domain tapers, and w is the parameter of the windowed frequency response $\mathcal{H}^{(\mathbf{G}_w)}[k_\mathrm{t},k_\mathrm{f};n,p]$. For more detailed information on the calculation of $\mathcal{H}^{(\mathbf{G}_w)}[k_\mathrm{t},k_\mathrm{f};n,p]$ please refer to Appendix B.

In [3], [37], the shortest stationarity time within our data set was determined to be $40\,\mathrm{ms}$ which relates to $M = 128$. Throughout this paper we stick to this minimum stationarity time to ensure that the statistical assumption of stationarity is fulfilled. The parameters selected for analyzing the measurements in this paper are $M = 128$ and $N = 769$, which results in a stationarity region of about $40\,\mathrm{ms} \times 240\,\mathrm{MHz}$. Note that we assume the channel is stationary over the total measured bandwidth. Hence, there are $K_\mathrm{t} = S/M = 250$ stationarity regions over the measurement time interval of $T = 10\,\mathrm{s}$. The obtained delay resolution $\tau_\mathrm{s} = 1/B = 4.17\,\mathrm{ns}$ and the Doppler resolution $\nu_\mathrm{s} = 1/\left(t_\mathrm{s}(M-1)\right) = 25.63\,\mathrm{Hz}$.

Based on the LSF $\hat{\mathcal{C}}[k_\mathrm{t},k_\mathrm{f};n,p]$, the time-varying PDP

$$\hat{P}_\tau[k_\mathrm{t},k_\mathrm{f};n] = \frac{1}{M} \sum_{p=-M/2}^{M/2-1} \hat{\mathcal{C}}[k_\mathrm{t},k_\mathrm{f};n,p], \tag{23}$$

and the time-varying DSD

$$\hat{P}_\nu[k_\mathrm{t},k_\mathrm{f};p] = \frac{1}{N} \sum_{n=0}^{N-1} \hat{\mathcal{C}}[k_\mathrm{t},k_\mathrm{f};n,p], \tag{24}$$

can be estimated by projecting the LSF on the delay and Doppler axis. The time-varying PDP and DSD over the time interval of $T = 10\,\mathrm{s}$ are presented in [1]. We restrict our attention to the case where both vehicles are inside the tunnel. Hence, we limit the following analysis to the time interval $4\,\mathrm{s} \leq t \leq t = 9\,\mathrm{s}$.

VI. Numerical Results

A. Simulation Setup

A schematic view of the scenario for the TX and RX position at $m = 0$ is shown in Fig. 4. Dimensions of the tunnel and the objects inside are taken from [46] and from a video recorded during the measurements.

1) Ray Tracing Settings: Each block is modeled as a perpendicular parallelepiped in RT. The true length of the tunnel is longer than the $586\,\mathrm{m}$ used in the RT model. The reason for the reduced length is that propagation paths from deep inside the tunnel, would be weak, but accounting for these would demand an extremely high computational effort. The dielectric properties are included in the input database of RT. Blocks made of metal are assumed to be perfect electric conductors. The values of relative permittivity ε_r, conductivity σ, scattering coefficient S and the integer α indicating the width of the scattering lobe of different materials are presented in Table II. According to the simulation parameters, dS is $1.23\,\mathrm{m}^2$ for the proposed subdivision algorithm based on (5).

According to (21), we deal with a single-input single-output V2V channel. Both the TX and RX antennas used for the RT simulation are half-wavelength dipole antennas. RT takes into account the following propagation mechanisms: LOS, reflections up to the fourth order, single-order diffraction and single bounce scattering. Exemplary propagation paths are visualized in Fig. 4(a). We select up to fourth order of reflection to obtain tractable computational complexity for RT.

This article has been accepted for publication in a future issue of this journal, but has not been fully edited. Content may change prior to final publication. Citation information: DOI 10.1109/TVT.2018.2839980, IEEE Transactions on Vehicular Technology

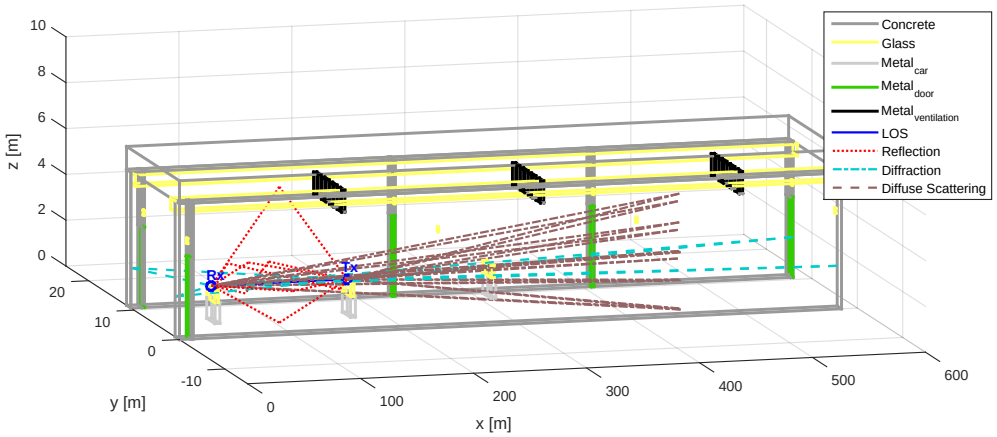

(a) 3D View

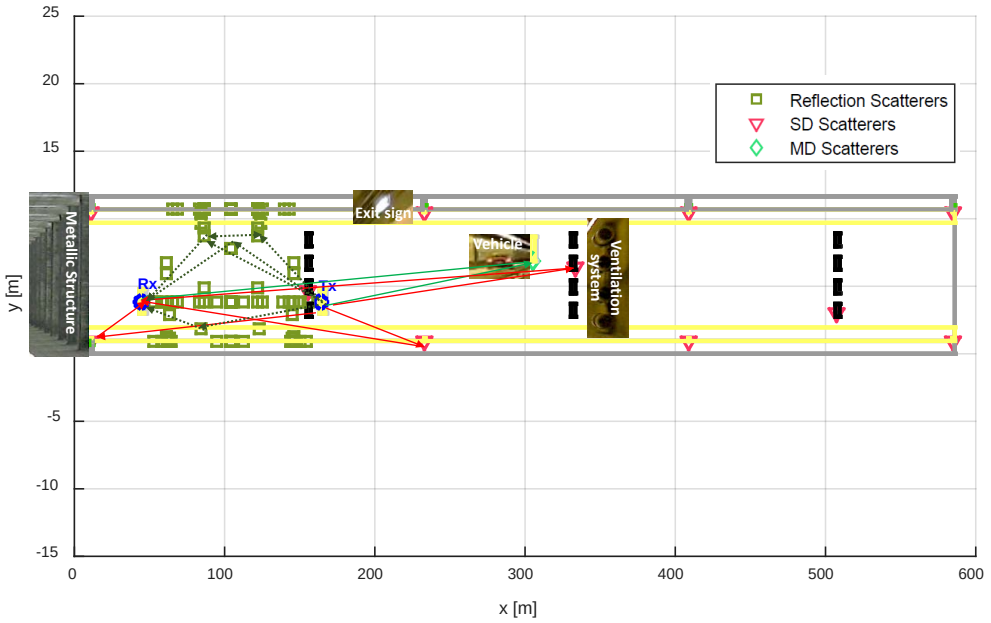

(b) 2D View

Fig. 4. Schematic view of the scenario built by RT considering TX and RX positions at time index $m = 0$. Line colors indicate type of material. (a) 3D view. (b) 2D view.

It is noteworthy that we do not consider the contributions from the ventilation system, EXIT signs, the metallic structure and the moving vehicle in RT. These elements are depicted and labeled in Fig. 4(b). The reason is that these blocks have small sizes or irregular shapes and their sizes and positions are not exactly known. Therefore, these blocks are considered in the propagation graph as described below.

2) Propagation Graph Settings: The parameter settings for the propagation graph are summarized in Table III. Below we introduce the scatterer positions, the probability of visibility and the edge gain.

Positions of Scatterers Vertices: The scatterers in the propagation graph for $m = 0$ are shown in Fig. 4(b), where different scatterer types are marked with different colors. The IP positions are directly obtained by RT from all reflection IPs.

TABLE II
PARAMETER SETTINGS FOR THE RT

Parameter	Setting			
Tunnel Size	$586 \times 11.65 \times 6.93$ m^3			
Reflect. order	$n_{\mathrm{RT}} = 4$			
Tile size	$dS = 1.23\,\mathrm{m}^2$			
Material	ε_r	σ (S/m)	S	α
Concrete	8.92	0.046	0.7	3
Glass	3.7	0	0.3	3

The number of IPs, N_{IP}, is different for different stationarity regions. Twelve SD scatterers ($N_{\mathrm{SD}} = 12$) are defined in the propagation graph, corresponding to three SD scatterers on the ventilation systems, eight SD scatterers on the EXIT signs and one SD scatterer on the big metallic structure at the entrance. We put SD scatterers on i) blocks made of metal or

This article has been accepted for publication in a future issue of this journal, but has not been fully edited. Content may change prior to final publication. Citation information: DOI 10.1109/TVT.2018.2839980, IEEE Transactions on Vehicular Technology

TABLE III
PARAMETER SETTINGS FOR THE PROPAGATION GRAPH

Parameter	Symbol	Setting
Propagation path order	n_{PG}	2
Number of SD scatterers	N_{SD}	12
Number of MD scatterers	N_{MD}	1
Min. distance threshold	$d_{\mathrm{th,min}}$	3.1 m
Max.distance threshold	$d_{\mathrm{th,max}}$	36 m
Reflection tail slope	$\hat{\rho}$	-72 dB/μs
Probability of visibility	P_{vis}	0.8

glass, which are important reflectors in the scenario, ii) the ventilation system and the big metallic structure which are hard to describe accurately by RT due to their irregular shapes, and iii) the EXIT signs that are small in size. Moreover, there is one MD scatterer ($N_{\mathrm{MD}} = 1$) on an additional moving vehicle, which is in front of the RX vehicle during the simulation period with a velocity of $v_{\mathrm{MD}} = 115$ km/h.

The generation of these discrete scatterers resembles the concept of a GSCM. The number of scatterers generated on one object is determined by the size and material of the object. The objects considered are small compared to the length of the tunnel. Moreover, both static and mobile objects in the present scenario are made of metal or glass, where reflection or diffraction are more likely to occur than at diffuse surfaces. However, a precise description of their geometry and position is unavailable. For this reason, we cannot determine the accurate reflection or diffraction interaction points. Therefore, we represent these objects by one random scatterer. Note that if larger objects of concrete are considered in the propagation graph, where diffuse scattering is more likely to occur, we can assign the number of scatterers according to the subdivision algorithm that was presented in Section III.

Positions of SD and MD scatterers are generated in the following way: i) The geometrical information of relevant blocks is defined. ii) We place one SD or MD scatterer randomly on one surface of the mentioned block, where a surface is selected randomly at $m = 0$. The selected surface cannot be one that is masked by any other blocks or surfaces. iii) The IPs and SD scatterers' positions are updated for every stationarity region k_{t} based on the RT result and the geometrical information of the scenario. The MD scatterer's position is updated for every time index m' based on its velocity. In Fig. 4(b), both the SD and MD scatterers' positions $\mathbf{r}_v$ at time index $m = 0$, located on the relevant blocks, are shown.

Edge Presence: Some examples of edges are shown in Fig. 4(b). We set $P_{\mathrm{vis}} = 0.8$ as in [28]. For obtaining the visibility between IPs based on (14) and (15), we define distance thresholds $d_{\mathrm{th,min}}$ and $d_{\mathrm{th,max}}$. As described in Section V, the LOS path length is 120 m. The longest reflection path length calculated by RT is $d_{\mathrm{ref,max}} = 126.2$ m at $m = 0$. We approximate $d_{\mathrm{th,min}}$ and $d_{\mathrm{th,max}}$ to be $d_{\mathrm{th,min}} = (126.2 - 120)/2 = 3.1$ m and $d_{\mathrm{th,max}} = 36$ m, where $d_{\mathrm{th,max}}$ is determined by the average distance between any two IPs $v \in \mathcal{V}_{\mathrm{IP}}$ at $m = 0$. When the condition in (15) is fulfilled, it confirms that propagation paths calculated based on RT and those based on the propagation graph cannot overlap with each other. It further provides the reason why we can set $n_{\mathrm{PG}} = 2$ in the propagation graph when $n_{\mathrm{RT}} = 4$ in RT.

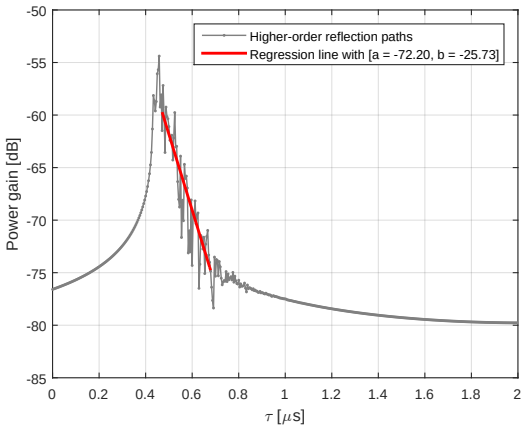

Fig. 5. Power-delay profile plot based on the approximate higher-order reflection algorithm and a corresponding least-squares linear regression line.

Edge Gain: For the edge gain g_e listed in Table I, the edge weight $S_{e,\{\cdot\}}$ and edge gain g_{II} are calculated according to (18) and (19), respectively. Depending on our settings, the relevant parameters are $\mathrm{odi}_{\mathrm{TS}}(e) = \mathrm{idi}_{\mathrm{SR}}(e) = 11$ and $\mathrm{odi}_{\mathrm{TM}}(e) = \mathrm{idi}_{\mathrm{MR}}(e) = 1$. Therefore, $S_{e,\mathrm{TS}} = S_{e,\mathrm{SR}} = 0.30$ and $S_{e,\mathrm{TM}} = S_{e,\mathrm{MR}} = 1$.

For different IP scatterers $\mathrm{odi}_{\mathrm{II}}(e)$ has different values and it changes for different stationarity regions, which results in a time-varying $S_{e,\mathrm{II}}$. From the simulation of the approximate higher-order reflection algorithm, we estimate $\hat{\rho} = -72\,\mathrm{dB}/\mu\mathrm{s}$ to obtain g_{II} from (19).

In the following analysis we compare the simulation results with measurements for a time interval of $T = 5$ s containing $K_{\mathrm{t}} = 125$ stationarity regions. The hybrid model is calculated once for each stationarity region $k_{\mathrm{t}} \in \{1, \ldots, K_{\mathrm{t}}\}$. From (2), we obtain $H_{\mathrm{HY}}[m, q]$. The CTFs $H_{\mathrm{RT}}[m', q]$ and $H_{\mathrm{PG}}[m', q]$ for $m' \in \{0, ..., 127\}$ can be obtained by using (7) and (10) for each stationarity region $k_{\mathrm{t}} \in \{1, \ldots, K_{\mathrm{t}}\}$, respectively.

B. Simulation Time

Due to the particular implementation of RT, it is hard to calculate the computational complexity. Therefore, we resort to an evaluation of the simulation time (2.4 GHz Intel Core i7 CPU with 8 GB RAM). The simulation time for obtaining the time-varying CTF $H_{\mathrm{RT}}[m', q, k_{\mathrm{t}}]$ for one stationarity region is 51 s, in which calculating deterministic paths and diffuse scattering paths takes 6 s and 45 s respectively. Moreover, the simulation time for obtaining the time-varying CTF $H_{\mathrm{PG}}[m, q]$ for one stationarity region takes 21 s. In total, the proposed hybrid model takes about 72 s to get the time-varying CTF $H[m', q, k_{\mathrm{t}}]$ for one stationarity region.

C. Analysis of Time-Varying PDP and DSD

The normalized time-varying PDP $\hat{P}_{\mathrm{MEA},\tau}[k_{\mathrm{t}}; n]$ and DSD $\hat{P}_{\mathrm{MEA},\nu}[k_{\mathrm{t}}; p]$ obtained from channel measurements, calculated according to (23) and (24), are shown in Fig. 6(a)

This article has been accepted for publication in a future issue of this journal, but has not been fully edited. Content may change prior to final publication. Citation information: DOI 10.1109/TVT.2018.2839980, IEEE Transactions on Vehicular Technology

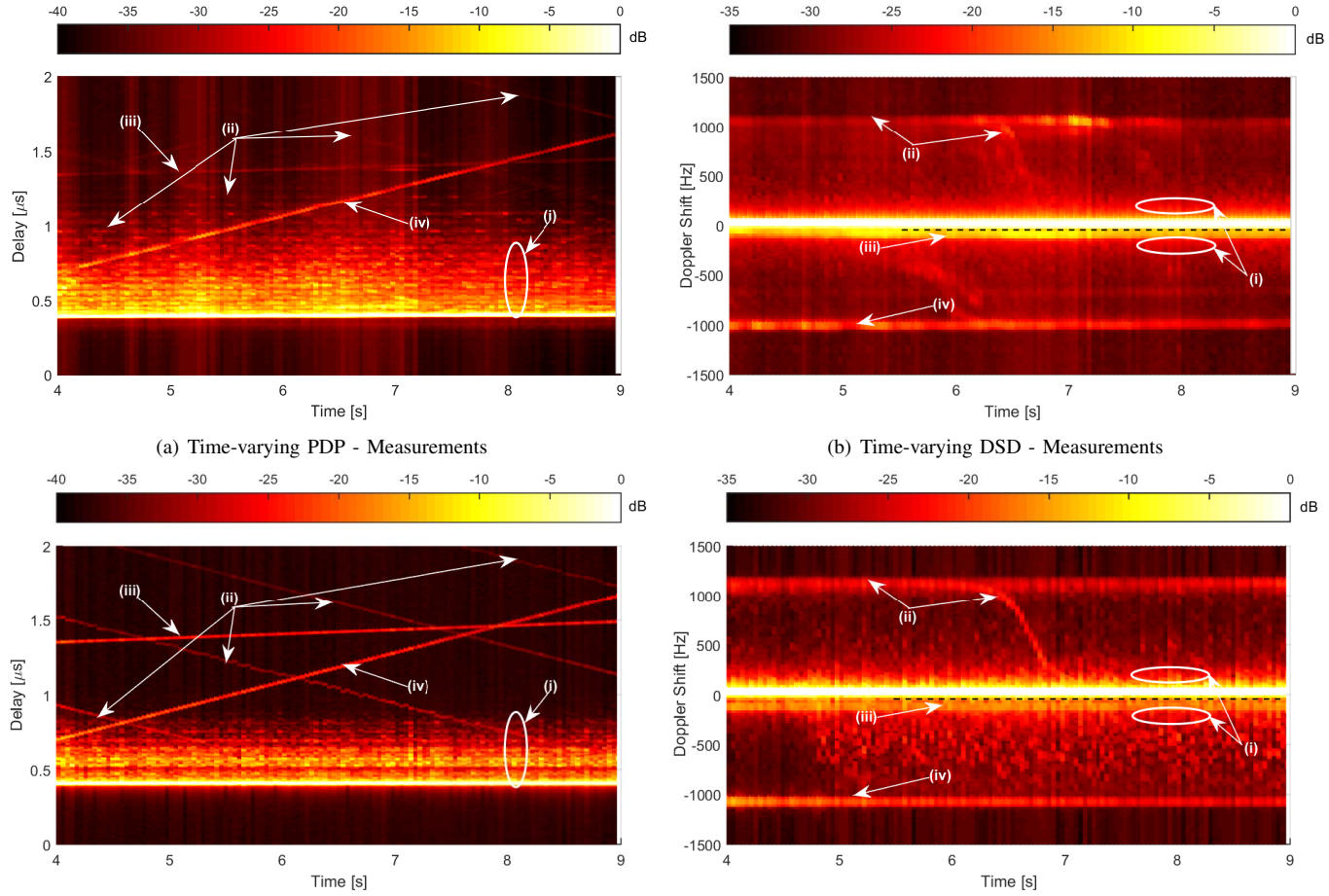

(a) Time-varying PDP - Measurements

(b) Time-varying DSD - Measurements

(c) Time-varying PDP - Hybrid Model

(d) Time-varying DSD - Hybrid Model

Fig. 6. Normalized time-varying PDP and DSD obtained from measurements and the proposed hybrid channel model over interval of $T = 5\,\mathrm{s}$, where $t = 4\,\mathrm{s}, \ldots, 9\,\mathrm{s}$. The contributions are from: (i) the higher-order reflection caused by the tunnel walls, ceiling and ground, (ii) the ventilation system and traffic signs in front of the RX, (iii) the car driving approximately 10 km/h faster than the TX and RX, and (iv) a big metallic structure at the entrance ceiling and traffic signs which are behind the RX.

and Fig. 6(b). The estimated normalized time-varying PDP $\hat{P}_{\mathrm{HY},\tau}[k_{\mathrm{t}}; n]$ and DSD $\hat{P}_{\mathrm{HY},\nu}[k_{\mathrm{t}}; p]$ of the proposed hybrid channel model are shown in Fig. 6(c) and Fig. 6(d). The measured time-varying channel transfer function has a signal-to-noise ratio (SNR) of roughly $40\,\mathrm{dB}$. In order to make a reasonable comparison with the measurement data, we add white Gaussian noise $n[m, q]$ with variance $\sigma_n^2 = \frac{1}{\mathrm{SNR}}$ with $\mathrm{SNR} = 40\,\mathrm{dB}$ in the simulation.

The contribution from objects inside the tunnel are clearly distinguishable. Comparing our simulation result with the time-varying PDP and DSD obtained from measurements, it can be seen that our simulation results provides a very accurate prediction of the measured data. The following propagation phenomena are highlighted: (i) higher-order reflection components which are mainly caused by the tunnel walls, ceiling and floor, (ii) multipath components from the ventilation system and from traffic signs in front of the RX, (iii) multipath components caused by a vehicle driving approximately 10 km/h faster than the TX and RX, and (iv) strong multipath components caused by a big metallic structure at the entrance ceiling and traffic signs that are behind the RX.

In Fig. 7, we focus on one stationarity region and compare the PDP and DSD of the proposed hybrid model with empirical channel measurement data. Some important features in the plots are marked by (i)–(iv). From Fig. 7(a), it appears that the proposed hybrid model agrees well with the measurements in terms of the PDP. The peaks (ii), (iii), and (iv) are mainly caused by the big metallic structure behind the RX, the ventilation system in front of the RX, the moving vehicle, and the traffic signs in front of the RX. The power of the path (iii) 6 dB higher than the same path in the measurement, which is due to the simplicity of the definition of the edge weight in our simulation. However, the same path seen in Fig. 7(b) is similar to the one in the measurement, because the diffuse scattering also contributes to the single path of the MD scatterer (iii). Moreover, it can be seen that the gain of diffuse scattering components, appearing between $0.4\,\mu\mathrm{s}$ and $0.5\,\mu\mathrm{s}$, is higher than the noise floor in Fig. 7(a). In addition, it can be observed from Fig. 7(b) that diffuse scattering components play an important role in the DSD evaluation, as their power is higher than the noise power.

This article has been accepted for publication in a future issue of this journal, but has not been fully edited. Content may change prior to final publication. Citation information: DOI 10.1109/TVT.2018.2839980, IEEE Transactions on Vehicular Technology

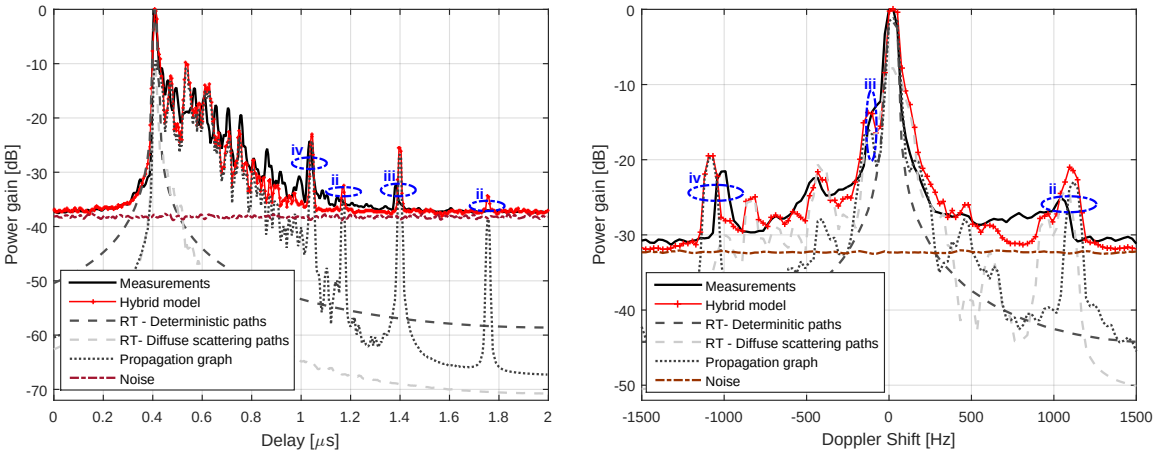

(a) Time-varying PDP at $k_\mathrm{t} = 45$

(b) Time-varying DSD at $k_\mathrm{t} = 45$

Fig. 7. Normalized time-varying PDP and DSD based on the tunnel RT algorithm at stationarity region $k_\mathrm{t} = 45$. The contributions are from: (ii) the ventilation system and traffic signs in front of the RX, (iii) the car driving approximately 10 km/h faster than the TX and RX, and (iv) a big metallic structure at the entrance ceiling and traffic signs which are behind the RX.

D. Analysis of Time-Varying Delay- and Doppler-Spread

The time-varying RMS delay spread is defined as [3]

$$\sigma_\tau[k_\mathrm{t}] = \sqrt{\frac{\sum_{n=0}^{N-1}(n\tau_\mathrm{s})^2\hat{P}_\tau[k_\mathrm{t};n]}{\sum_{n=0}^{N-1}\hat{P}_\tau[k_\mathrm{t};n]} - \bar{\tau}[k_\mathrm{t}]^2}, \tag{25}$$

with

$$\bar{\tau}[k_\mathrm{t}] = \frac{\sum_{n=0}^{N-1}(n\tau_\mathrm{s})\hat{P}_\tau[k_\mathrm{t};n]}{\sum_{n=0}^{N-1}\hat{P}_\tau[k_\mathrm{t};n]}. \tag{26}$$

The time-varying RMS Doppler spread $\sigma_\nu[k_\mathrm{t}]$ is defined similarly, please see [3].

In order to eliminate noise components that could be mistaken as multipath components, we set all the components to zero whose power is not more than 5 dB higher than the noise power [1], [3]. We compare estimates of the RMS delay spreads of measurements and simulations in Fig. 8(a). The RMS delay spread of the measurement fluctuates around $0.1\,\mu$s. The proposed hybrid channel model provides a similar trend and mean value as the measurements. RT with deterministic paths only provides a smaller value $\sigma_\tau = 0.004\,\mu$s, and RT with deterministic and diffuse scattering paths provides a similar value for σ_τ of around $0.004\,\mu$s. To reduce computational complexity further we omit the diffuse scattering paths in the hybrid model, i.e., we consider only RT and the propagation graph contributions. Here, we observe a good match to the hybrid model in terms of the RMS delay spread. Thus, the diffuse scattering paths simulated with RT do not influence the RMS delay spread significantly in our case.

Moreover, we compare the RMS Doppler spreads of measurements and simulations in Fig. 8(b). The RMS Doppler spread of the measurement fluctuates around 170 Hz. Our proposed hybrid channel model gives a similar mean value as the measurement. RT with deterministic paths only gives a smaller σ_ν around 70 Hz, while RT with deterministic and diffuse scattering paths gives a similar σ_ν value to the proposed hybrid channel model. When considering deterministic paths in RT and the propagation paths generated by the propagation graph, σ_ν is slightly lower than the proposed hybrid channel model. Moreover, combing with the observation in Fig. 7(b), we conclude that the contribution from diffuse scattering paths is important in the RMS Doppler spread analysis[3].

VII. Conclusion

In this paper, we presented a hybrid channel model for modeling non-stationary time-variant vehicle-to-vehicle in-tunnel channels. The hybrid model combines ray tracing with the propagation graph model to yield a novel channel model for in-tunnel environments with reduced computational complexity. Ray tracing is enhanced with an effective subdivision algorithm for diffuse scattering. We include the time evolution of the relevant parameters in the proposed model, based on the local scattering function defined for a local region of stationarity. For each stationarity region we compute the time evolution of each propagation path with the sum of complex exponential algorithm, which reduces the computational complexity considerably.

The propagation graph generates not only the reflection tail, but also the contributions from other important static discrete and mobile discrete scatterers in the tunnel. All vertices for the propagation graph are obtained from ray tracing. Static discrete and mobile discrete scatterers are randomly generated on small or irregular shaped objects, whose exact locations are unknown. In case of such incomplete information for ray tracing, we propose to include them in the propagation graph as stochastically placed vertices. The number of scatterers generated on one object depends on the size and the material of the object. The static discrete scatterer locations are updated

[3]It should be remarked that in this paper we aim at giving an overview of all contributions of the proposed model. However, for balancing the computational time and accuracy, it should be considered whether diffuse scattering can be neglected in some applications.

This article has been accepted for publication in a future issue of this journal, but has not been fully edited. Content may change prior to final publication. Citation information: DOI 10.1109/TVT.2018.2839980, IEEE Transactions on Vehicular Technology

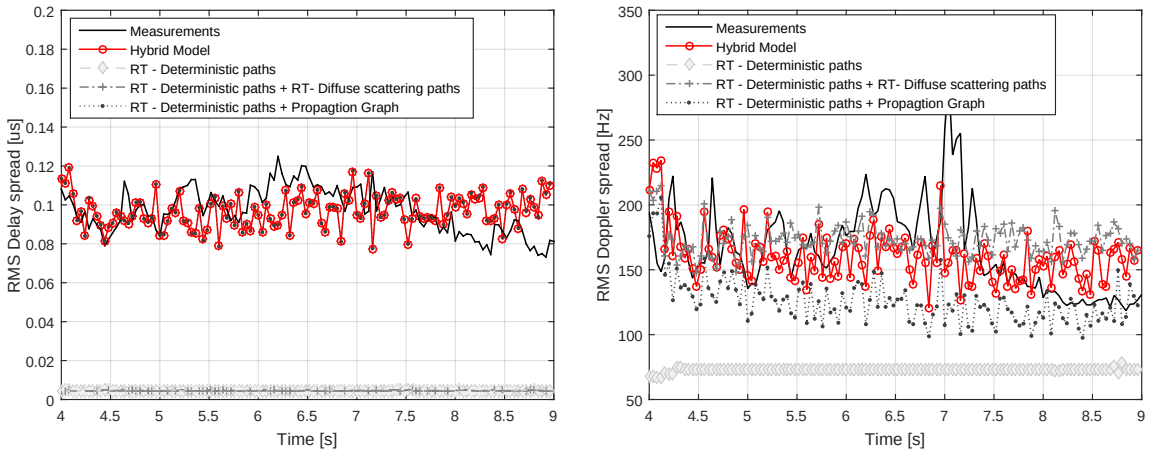

(a) RMS Delay Spread

(b) RMS Doppler Spread

Fig. 8. Time-varying RMS delay and Doppler spreads comparison.

for every stationarity region based on the ray tracing results, while the mobile discrete scatterers locations are updated for every time index based on their speed.

The accuracy of the proposed algorithm was verified by comparison with empirical channel measurement data. Our proposed hybrid model allowed us to obtain comparable power delay profiles, Doppler power spectral densities, root mean square delay- and Doppler-spreads. We also showed that the contribution from the diffuse scattering paths plays an important role in the Doppler power-spectral density and root mean-square Doppler spread evaluation.

Appendix A
Transfer Functions of the Propagation Graph

Closed-form expressions for the full and partial transfer functions of a propagation graph are derived in [26]. The expression for the full transfer function

$$\mathbf{H}_{\text{PG}}[q] = \mathbf{D}[q] + \mathbf{R}[q]\left[\mathbf{I} - \mathbf{B}[q]\right]^{-1}\mathbf{T}[q] \tag{27}$$

was derived considering the interaction order to be unbounded. Moreover, a closed form expression was given for the partial transfer function $\mathbf{H}_{\text{PG},K:L}[q]$ with interaction order at least K and at most L. Some special cases include:

$$\begin{aligned}
\mathbf{H}_{\text{PG},0:L}[q] &= \mathbf{D}[q] + \mathbf{R}[q]\left[\mathbf{I} - \mathbf{B}^{L}[q]\right]\left[\mathbf{I} - \mathbf{B}[q]\right]^{-1}\mathbf{T}[q], \\
\mathbf{H}_{\text{PG},K:L}[q] &= \mathbf{R}[q]\left[\mathbf{B}^{K-1}[q] - \mathbf{B}^{L}[q]\right]\left[\mathbf{I} - \mathbf{B}[q]\right]^{-1}\mathbf{T}[q], \\
\mathbf{H}_{\text{PG},K:\infty}[q] &= \mathbf{R}[q]\mathbf{B}^{K-1}[q]\left[\mathbf{I} - \mathbf{B}[q]\right]^{-1}\mathbf{T}[q]
\end{aligned} \tag{28}$$

for $K \geq 1$. Detailed proofs of (27) and (28) are given in [26].

Appendix B
Windowed Frequency Response

The windowed frequency response [3] $\mathcal{H}^{(G_w)}[k_t, k_f; n, p]$ is defined as

$$\mathcal{H}^{(G_w)}[k_t, k_f; n, p] = \sum_{m''=-M/2}^{M/2-1}\sum_{q''=-N/2}^{N/2-1} H[m'' - k_t, q'' - k_f] \\ G_w[m'', q'']\mathrm{e}^{-\mathrm{i}2\pi(pm''-nq'')}. \tag{29}$$

where the relative time index m'' within each stationarity region is $m'' = m' - M/2$, so that $m'' \in [-M/2, M/2-1]$. The relative frequency index within each stationary frequency region is $q'' \in \{-N/2, \ldots, N/2-1\}$. The window function $G_w[m'', q'']$ is well localized within the support region $[-M/2, M/2-1] \times [-N/2, N/2-1]$. The discrete time equivalent of the separable frequency response used in [45] is applied, $G_w[m'', q''] = u_i[m'' + M/2]\tilde{u}_j[q'' + N/2]$ where $w = iJ + j$, $i \in \{0, \ldots, I-1\}$, and $j \in \{0, \ldots, J-1\}$. The sequences $u_i[m'']$ and $\tilde{u}_j[q'']$ are chosen as the discrete prolate spheroidal sequence (DPSSs) [47], [48] with concentration in the interval $\mathcal{I}_M = \{0, \ldots, M-1\}$ and bandlimited to $[-I/M, I/M]$, and in the interval $\mathcal{I}_N = \{0, \ldots, N-1\}$ and bandlimited to $[-J/N, J/N]$, respectively.

Appendix C
Approximate Higher-Order Reflection Algorithm

In tunnel structures the guiding effect can be a dominant propagation process. Such a process arises due to multiple reflections of paraxial rays on the tunnel's walls, which can become important because of the long shape of such structures and of the reflection coefficients' amplitude tending to one for grazing incidence. Such a guiding effect can be modeled by using RT with many reflections. However, the computational complexity of RT increases exponentially with reflection order. Therefore, we resort to the propagation graph model in this work and use the low-complexity approximate higher-order reflection algorithm from [49] to tune the propagation graph parameter set.

The approximate higher-order reflection algorithm treats the tunnel as an equivalent rectangle [49]. The input for the algorithm includes the positions of TX and RX, the width and the height of the tunnel, as well as the permittivity and conductivity of the vertical and horizontal walls. The propagation paths experiences multiple vertical and horizontal reflections. For a certain path with a given reflection order, all incidence angles on the vertical and horizontal walls, remain the same. Based on the TX position, the coordinate of the image point and the complex electric field for the reflection

paths can be calculated. We use the result shown in Fig. 5 to obtain the slope of the PDP which is needed as parameter for the propagation graph model. For the calculation of Fig. 5 we used 40 reflections, according to [50]. For more detailed information, please refer to [23].

REFERENCES

[1] L. Bernadó, A. Roma, A. Paier, T. Zemen, N. Czink, J. Kåredal, A. Thiel, F. Tufvesson, A. F. Molisch, and C. F. Mecklenbräuker, "In-tunnel vehicular radio channel characterization," in *IEEE 73rd Vehicular Technology Conference (VTC Spring)*, May 2011, pp. 1–5.

[2] "Simulation and measurement based vehicle-to-vehicle channel characterization: Accuracy and constraint analysis," in *IEEE Transactions on Antennas and Propagation*, vol. 63, no. 7, July 2015, pp. 3208–3218.

[3] L. Bernadó, T. Zemen, F. Tufvesson, A. F. Molisch, and C. Mecklenbräuker, "Delay and Doppler spreads of nonstationary vehicular channels for safety-relevant scenarios," in *IEEE Transactions on Vehicular Technology*, vol. 63, no. 1, January 2014, pp. 82–93.

[4] A. E. Forooshani, S. Bashir, D. G. Michelson, and S. Noghanian, "A survey of wireless communications and propagation modeling in underground mines," in *IEEE Communications Surveys Tutorials*, vol. 15, no. 4, Fourth Quarter 2013, pp. 1524–1545.

[5] A. Hrovat, G. Kandus, and T. Javornik, "A survey of radio propagation modeling for tunnels," in *IEEE Communications Surveys Tutorials*, vol. 16, no. 2, Second Quarter 2014, pp. 658–669.

[6] K. Guan, B. Ai, A. Fricke, D. He, Z. Zhong, D. W. Matolak, and T. Kürner, "Excess propagation loss modeling of semiclosed obstacles for intelligent transportation system," *IEEE Transactions on Intelligent Transportation Systems*, vol. 17, no. 8, pp. 2171–2181, Aug. 2016.

[7] Y. Liu, A. Ghazal, C. X. Wang, G. E. Xiaohu, Y. Yang, and Y. Zhang, "Channel measurements and models for high-speed train wireless communication systems in tunnel scenarios: A survey," *Science China*, vol. 60, no. 10, p. 101301, Oct. 2017.

[8] Y. Liu, C. X. Wang, C. Lopez, and X. Ge, "3d non-stationary wideband circular tunnel channel models for high-speed train wireless communication systems," *Science China Information Sciences*, vol. 60, no. 8, p. 082304, Aug. 2017.

[9] Y. P. Zhang, "Novel model for propagation loss prediction in tunnels," in *IEEE Transactions on Vehicular Technology*, vol. 52, no. 5, September 2003, pp. 1308–1314.

[10] A. Hrovat, G. Kandus, and T. Javornik, "Four-slope channel model for path loss prediction in tunnels at 400 MHz," in *IET Microwaves, Antennas and Propagation*, vol. 4, no. 5, May 2010, pp. 571–582.

[11] Y. Yuan, C. X. Wang, X. Cheng, B. Ai, and D. I. Laurenson, "Novel 3d geometry-based stochastic models for non-isotropic mimo vehicle-to-vehicle channels," *IEEE Transactions on Wireless Communications*, vol. 13, no. 1, pp. 298–309, Jan. 2014.

[12] Y. Yuan, C. X. Wang, Y. He, M. M. Alwakeel, and e. H. M. Aggoune, "3d wideband non-stationary geometry-based stochastic models for non-isotropic mimo vehicle-to-vehicle channels," *IEEE Transactions on Wireless Communications*, vol. 14, no. 12, pp. 6883–6895, Dec. 2015.

[13] S.-H. Chen and S.-K. Jeng, "SBR image approach for radio wave propagation in tunnels with and without traffic," in *IEEE Transactions on Vehicular Technology*, vol. 45, no. 3, August 1996, pp. 570–578.

[14] M. H. Kermani and M. Kamarei, "A ray-tracing method for predicting delay spread in tunnel environments," in *IEEE International Conference on Personal Wireless Communication*, December 2000, pp. 538–542.

[15] D. Didascalou, T. M. Schafer, F. Weinmann, and W. Wiesbeck, "Ray-density normalization for ray-optical wave propagation modeling in arbitrarily shaped tunnels," in *IEEE Transactions on Antennas and Propagation*, vol. 48, no. 9, September 2000, pp. 1316–1325.

[16] F. M. Pallares, F. J. P. Juan, and L. Juan-Llacer, "Analysis of path loss and delay spread at 900 MHz and 2.1 GHz while entering tunnels," in *IEEE Transactions on Vehicular Technology*, vol. 50, no. 3, May 2001, pp. 767–776.

[17] J. Molina-Garcia-Pardo, J.-V. Rodriguez, and L. Juan-Llacer, "Wideband measurements and characterization at 2.1 GHz while entering in a small tunnel," in *IEEE Transactions on Vehicular Technology*, vol. 53, no. 6, November 2004, pp. 1794–1799.

[18] Y. P. Zhang and Y. Hwang, "Characterization of UHF radio propagation channels in tunnel environments for microcellular and personal communications," in *IEEE Transactions on Vehicular Technology*, vol. 47, no. 1, February 1998, pp. 283–296.

[19] S. F. Mahmoud, "On modal propagation of high frequency electromagnetic waves in straight and curved tunnels," in *IEEE Antennas and Propagation Society International Symposium*, vol. 3, June 2004, pp. 2963–2966.

[20] M. M. Rana and A. S. Mohan, "Segmented-locally-one-dimensional-FDTD method for EM propagation inside large complex tunnel environments," in *IEEE Transactions on Magnetics*, vol. 48, no. 2, February 2012, pp. 223–226.

[21] P. Bernardi, D. Caratelli, R. Cicchetti, V. Schena, and O. Testa, "A numerical scheme for the solution of the vector parabolic equation governing the radio wave propagation in straight and curved rectangular tunnels," in *IEEE Transactions on Antennas and Propagation*, vol. 57, no. 10, October 2009, pp. 3249–3257.

[22] F. Fuschini and G. Falciasecca, "A mixed rays - modes approach to the propagation in real road and railway tunnels," in *IEEE Transactions on Antennas and Propagation*, vol. 60, no. 2, February 2012, pp. 1095–1105.

[23] M. Gan, Z. Xu, V. Shivaldova, A. Paier, F. Tufvesson, and T. Zemen, "A ray tracing algorithm for intelligent transport systems in tunnels," in *IEEE 6th International Symposium on Wireless Vehicular Communications (WiVeC)*, September 2014, pp. 1–5.

[24] F. Mani, F. Quitin, and C. Oestges, "Accuracy of depolarization and delay spread predictions using advanced ray-based modeling in indoor scenarios," *EURASIP Journal on Wireless Communications and Networking*, vol. 2011, no. 1, p. 11, 2011. [Online]. Available: http://dx.doi.org/10.1186/1687-1499-2011-11

[25] T. Pedersen and B. H. Fleury, "A realistic radio channel model based in stochastic propagation graphs," in *5th Conf. on Mathematical Modelling (MATHMOD 2006)*, 2006, pp. 324–331.

[26] T. Pedersen, G. Steinböck, and B. H. Fleury, "Modeling of reverberant radio channels using propagation graphs," in *IEEE Transactions on Antennas and Propagation*, vol. 60, no. 12, December 2012, pp. 5978–5988.

[27] W. Cheng, C. Tao, L. Liu, R. Sun, and T. Zhou, "Geometrical channel characterization for high speed railway environments using propagation graphs methods," in *16th International Conference on Advanced Communication Technology (ICACT)*, Feb. 2014, pp. 239–243.

[28] T. Pedersen, G. Steinböck, and B. H. Fleury, "Modeling of outdoor-to-indoor radio channels via propagation graphs," in *XXXIth URSI General Assembly and Scientific Symposium (URSI GASS)*, August 2014, pp. 1–4.

[29] K. Stern, A. Fuglsig, K. Ramsgaard-Jensen, and T. Pedersen, "Propagation graph modeling of time-varying radio channels," 2018.

[30] G. Steinböck, M. Gan, P. Meissner, E. Leitinger, K. Witrisal, T. Zemen, and T. Pedersen, "Hybrid model for reverberant indoor radio channels using rays and graphs," in *IEEE Transactions on Antennas and Propagations*, vol. 64, no. 9, September 2016, pp. 4036–4048.

[31] L. Tian, V. Degli-Esposti, E. M. Vitucci, and X. Yin, "Semi-deterministic radio channel modeling based on graph theory and ray-tracing," *IEEE Transactions on Antennas and Propagation*, vol. 64, no. 6, pp. 2475–2486, June 2016.

[32] D. A. Hill, "A reflection coefficient derivation for the Q of a reverberation chamber," in *IEEE Transactions on Electromagnetic Compatibility*, vol. 38, no. 4, Nov. 1996, pp. 591–592.

[33] K. Guan, B. Ai, M. L. Nicolás, R. Geise, A. Möller, Z. Zhong, and T. Kürner, "On the influence of scattering from traffic signs in vehicle-to-x communications," *IEEE Transactions on Vehicular Technology*, vol. 65, no. 8, pp. 5835–5849, Aug 2016.

[34] J. Kåredal, F. Tufvesson, N. Czink, A. Paier, C. Dumard, T. Zemen, C. Mecklenbräuker, and A. F. Molisch, "A geometry-based stochastic MIMO model for vehicle-to-vehicle communications," in *IEEE Transactions on Wireless Communications*, vol. 8, no. 7, July 2009, pp. 3646 – 3657.

[35] L. Bernadó, T. Zemen, F. Tufvesson, A. Molisch, and C. Mecklenbräuker, "Time- and frequency-varying K-factor of non-stationary vehicular channels for safety relevant scenarios," vol. 16, no. 2, pp. 1007–1017, April 2015.

[36] G. Matz, "On non-WSSUS wireless fading channels," in *IEEE Transactions on Wireless Communications*, vol. 4, no. 5, September 2005, pp. 2465–2478.

[37] A. Paier, T. Zemen, L. Bernadó, G. Matz, J. Kåredal, N. Czink, C. Dumard, F. Tufvesson, A. F. Molisch, and C. F. Mecklenbräuker, "Non-WSSUS vehicular channel characterization in highway and urban scenarios at 5.2 GHz using the local scattering function," in *International ITG Workshop on Smart Antennas (WSA)*, February 2008, pp. 9–15.

[38] M. Gan, F. Mani, F. Kaltenberger, C. Oestges, and T. Zemen, "A ray tracing algorithm using the discrete prolate spheroidal subspace," in

This article has been accepted for publication in a future issue of this journal, but has not been fully edited. Content may change prior to final publication. Citation information: DOI 10.1109/TVT.2018.2839980, IEEE Transactions on Vehicular Technology

IEEE International Conference on Communications (ICC), June 2013, pp. 5710–5714.

[39] C. Oestges, B. Clerckx, L. Raynaud, and D. Vanhoenacker-Janvier, "Deterministic channel modeling and performance simulation of micro-cellular wide-band communication systems," in *IEEE Transactions on Vehicular Technology*, vol. 51, no. 6, November 2002, pp. 1422 – 1430.

[40] V. Degli-Esposti, F. Fuschini, E. M. Vitucci, and G. Falciasecca, "Measurement and modelling of scattering from buildings," in *IEEE Transactions on Antennas and Propagation*, vol. 55, no. 1, January 2007, pp. 143 – 153.

[41] M. Gan, X. Li, F. Tufvesson, and T. Zemen, "An effective subdivision algorithm for diffuse scattering of ray tracing," in *XXXIth URSI General Assembly and Scientific Symposium (URSI GASS)*, August 2014, pp. 1–4.

[42] M. Walter, D. Shutin, and U.-C. Fiebig, "Delay-dependent doppler probability density functions for vehicle-to-vehicle scatter channels," in *IEEE Transactions on Antennas and Propagation*, vol. 62, no. 4, April 2014, pp. 2238–2249.

[43] A. Paier, L. Bernadó, J. Kåredal, O. Klemp, and A. Kwoczek, "Overview of vehicle-to-vehicle radio channel measurements for collision avoidance applications," in *IEEE 71st Vehicular Technology Conference (VTC Spring)*, May 2010, pp. 1–5.

[44] A. Thiel, O. Klemp, A. Paiera, L. Bernadó, J. Karedal, and A. Kwoczek, "In-situ vehicular antenna integration and design aspects for vehicle-to-vehicle communications," in *Proceedings of the Fourth European Conference on Antennas and Propagation*, April 2010, pp. 1–5.

[45] G. Matz, "Doubly underspread non-WSSUS channels: analysis and estimation of channel statistics," in *IEEE 4th Workshop on Signal Processing Advances in Wireless Communications*, June 2003, pp. 190–194.

[46] C. Marshall, "The Øresund tunnel - making a success of design and build," in *Tunneling and Underground Space Technolody*, vol. 58, no. 3, 1999, pp. 355–365.

[47] D. Slepian, "Prolate spheroidal wave functions, fourier analysis, and uncertainty - V:the discrete case," in *The Bell System Technical Journal*, vol. 57, no. 5, 1978, pp. 1371 – 1430.

[48] D. J. Thomson, "Jackknifing multitaper spectrum estimates," *IEEE Signal Processing Magazine*, vol. 24, no. 4, pp. 20 – 30, July 2007.

[49] Z. Sun and I. F. Akyildiz, "Channel modeling and analysis for wireless networks in underground mines and road tunnels," in *IEEE Transactions on Communications*, vol. 58, no. 6, June 2010, pp. 1758–1768.

[50] C. Zhou, J. Waynert, T. Plass, and R. Jacksha, "Modeling RF propagation in tunnels," in *IEEE Antennas and Propagation Society International Symposium (APSURSI)*, July 2013, pp. 1916–1917.

Mingming Gan received the B.Sc. degree in electronic information engineering from Minzu University of China, China in 2007. She received the M.Sc. degree in wireless communications from Lund University, Sweden in 2010, with her Master Thesis written at the FTW Telecommunications Research Center Vienna, Austria. In 2015, she received her Ph.D. degree with distinction in engineering sciences from Vienna University of Technology, Austria. From 2010 to 2015, she was with the FTW Telecommunications Research Center Vienna working as a researcher in the "Signal and Information Processing" department. After working at AIT Austrian Institute of Technology as a researcher in the research group for ultra-reliable wireless machine-to-machine communications, Mingming joined Shanghai Huawei Technologies as a senior engineer in 2016. Her research interests are in the fields of modelling of wireless propagation channels, indoor channel characterization for high-speed short-range systems, time-variant vehicle-to-vehicle communications, time-variant fast fading statistics and diffuse scattering algorithms.

Gerhard Steinböck received the DI (FH) degree in telecommunications from Technikum Wien, Austria in 1999. From 2000 to 2006, he worked as a R&D engineer at the Austrian Institute of Technology (AIT), Vienna, Austria, contributing among other things in the hard- and software development of a real-time radio channel emulator. Gerhard Steinböck received the M.Sc.E. *(cum laude)* and the Ph.D. degree in wireless communications from Aalborg University, Denmark, in 2008 and 2013, respectively. After continuing as a postdoctoral researcher at Aalborg University, Gerhard Steinböck joined Huawei Technologies Sweden AB in 2016. His research interests lie in the area of wireless communications, systems simulation, radio channel modeling, radio channel estimation and sounding, and radio geolocation techniques.

Zhinan Xu received his M.Sc. degree in wireless communications from Lund university, Sweden in 2011 and Ph.D degree in telecommunications from Vienna University of Technology, Austria in 2016. From 2008 to 2009, he worked as mobile network engineer with Huawei Technologies, Shenzhen, China. From 2011 to 2015, he was with the Telecommunications Research Center Vienna (FTW) working as a researcher in "Signal and Information Processing" department. Since 2015 he has been with AIT Austrian Institute of Technology as a scientist in the research group for ultra-reliable wireless machine-to-machine communications. His research interests include interference management, cooperative communication systems, vehicular communications and channel modeling.

Troels Pedersen received the M.Sc. degree in digital communications and the Ph.D. degree in wireless communications from Aalborg University, Aalborg, Denmark, in 2004 and 2009, respectively. He has been with the Department of Electronic Systems, Aalborg University, since 2009, as an Assistant Professor, and since 2012, as an Associate Professor. In 2012, he was a Visiting Professor with IETR, Rennes, France, University Rennes 1, Rennes. His current research interests are within statistical signal processing and communication theory, including sensor array signal processing, radio geolocation techniques, radio channel modeling, and radio channel sounding. Dr. Pedersen received the Teacher of the Year Award twice by the Study Board for Electronics and IT, Aalborg University, in 2011 and 2017, respectively.

This article has been accepted for publication in a future issue of this journal, but has not been fully edited. Content may change prior to final publication. Citation information: DOI 10.1109/TVT.2018.2839980, IEEE Transactions on Vehicular Technology

Thomas Zemen (S'03-M'05-SM'10) received the Dipl.-Ing. degree (with distinction) in electrical engineering in 1998, the doctoral degree (with distinction) in 2004 and the Venia Docendi (Habilitation) for "Mobile Communications" in 2013, all from Vienna University of Technology. Since 2014 Thomas Zemen has been Senior Scientist at AIT Austrian Institute of Technology. He took on the role of Thematic Coordinator for physical layer security in 2018. From 2003 to 2014 he was with FTW Forschungszentrum Telekommunikation Wien and Head of the "Signal and Information Processing" department since 2008. From 1998 to 2003 Thomas Zemen worked as Hardware Engineer and Project Manager for the Radio Communication Devices Department, Siemens Austria. He is the author or coauthor of four books chapters, 35 journal papers and more than 105 conference communications. His research interests focus on wireless ultra-reliable low-latency communications (URLLC) system for autonomous vehicles and industrial production environments; 5G massive MIMO systems; time-variant channel measurements, modeling and real time emulation; software-defined radio rapid prototyping, and indoor localization. Dr. Zemen is an External Lecturer with the Vienna University of Technology and served as Editor for the IEEE Transactions on Wireless Communications from 2011 - 2017.